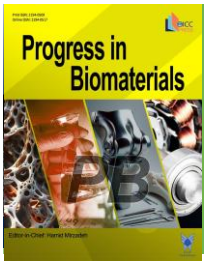

Volume 14, Issue 4, 2025: Article 23

Progress in Biomaterials (PIBM)

https://doi.org/10.57647/pibm.2025.1404.62

Dual-Layer Sponge–Nanofiber Construct Enabling Sustained Sitagliptin Release for Enhanced Diabetic Wound Healing

Roya Hesari Asl[1], Shahrokh Shojaei[1*], Mohammad Narimani Rad[1], Azadeh Asefnejad[2], Milad Jafari-Nodoushan[1]

[1]*Department of Biomedical Engineering, CT.C., Islamic Azad University, Tehran, Iran*
[2]*Department of Biomedical, Engineering, SR.C., Islamic Azad University, Tehran, Iran*

***Corresponding author:** shahrokhshojaei@iau.ir

Original Research:

Received:
30 October 2025

Accepted:
27 December 2025

Published in issue:
31 December 2025

Abstract

Diabetic wounds pose a major challenge due to impaired healing, infection risk, and poor vascularization. A Dual-layer biomimetic wound dressing was designed to integrate structural and biochemical functionalities for advanced wound management. The upper layer consisted of a sponge matrix based on polyacrylic acid and poly(allylamine hydrochloride), embedded with sitagliptin-loaded fucoidan–chitosan nanoparticles, enabling exudate absorption and sustained drug release. The lower layer comprised electrospun silk fibroin nanofibers, closely mimicking extracellular matrix architecture. Characterization was performed using SEM and FTIR. The dressing demonstrated a swelling ratio of 512.2% in distilled water and degradation of 38.2% after 7 days immersion in PBS. Sustained sitagliptin release reached 82.4% over 7 days. Mechanical evaluation revealed tensile strength of 354.0 KPa, elastic modulus of 987.6 KPa, and elongation of 171.3%, which was adequate for wound healing applications. *In vitro* assays confirmed superior L929 fibroblast viability on the Dual-layer dressing, with the nanofibrous layer supporting extensive adhesion and spreading. *In vivo* studies in a diabetic rat model showed enhanced re-epithelialization, organized collagen bundles, improved early-stage angiogenesis, and reduced inflammation, resulting in nearly complete wound healing within 14 days. These findings indicate that the Dual-layer dressing provides a promising strategy for diabetic wound healing.

Keywords: Chitosan; Diabetic wound healing; Dual-layer dressing; Fucoidan; Silk fibroin; Sitagliptin

Cite this article: Hesari Asl, R., Shojaei, Sh., Narimani Rad, M., Asefnejad, A., & Jafari-Nodoushan, M., Dual-Layer Sponge–Nanofiber Construct Enabling Sustained Sitagliptin Release for Enhanced Diabetic Wound Healing. Progress in Biomaterials 14(4), Article 23 (2025). https://doi.org/10.57647/pibm.2025.1404.62

Graphical abstract

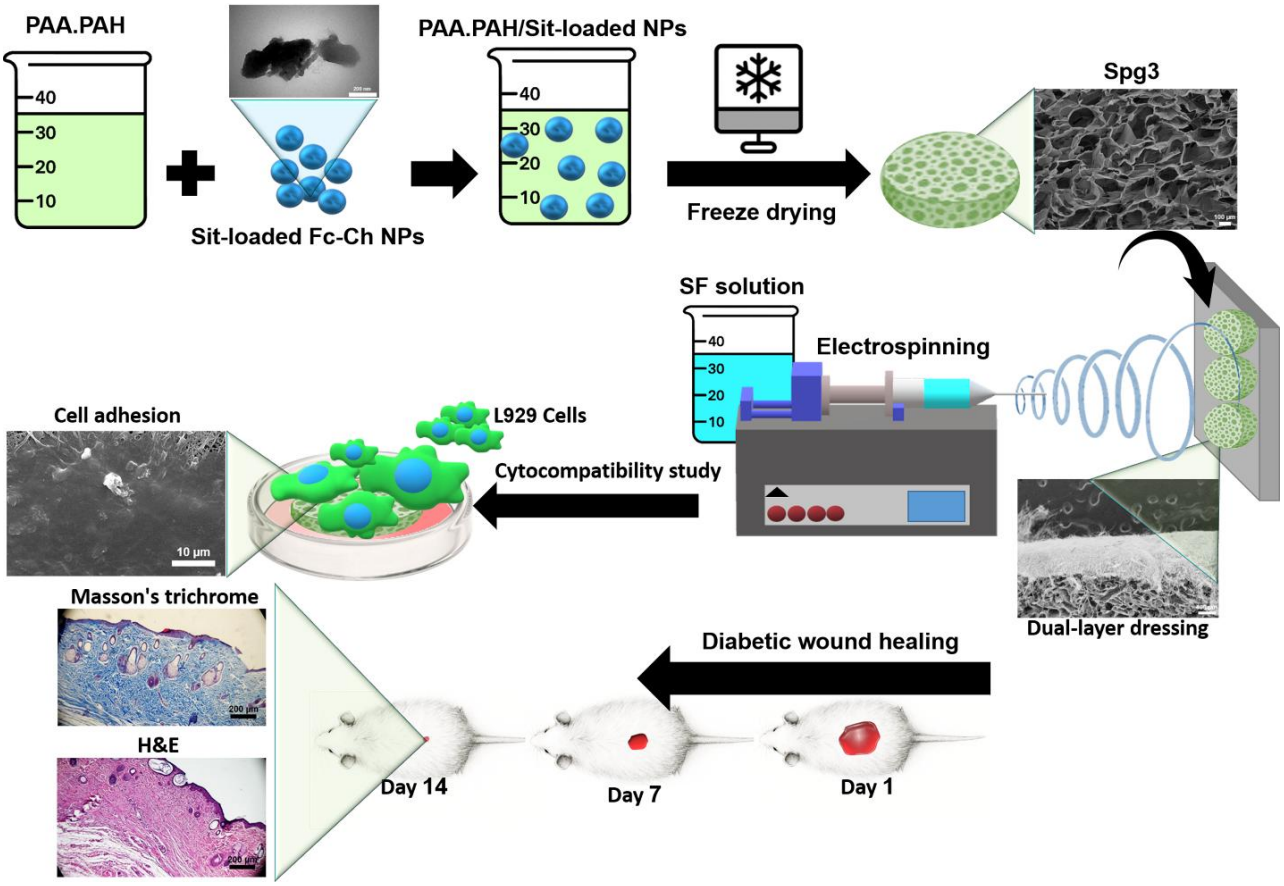

1. Introduction

Diabetic wounds pose a major global health and economic burden, with impaired healing mechanisms such as reduced cell migration, collagen synthesis, and angiogenesis, contributing to a high risk of chronic ulcers, limb amputation, and mortality [1]. Approximately 15% of individuals with diabetes experience foot ulcers, which contribute significantly to diabetes-related amputations [2].

Rapid healing of diabetic wounds requires a controlled microenvironment that supports cellular activity, prevents contamination, and maintains optimal moisture and temperature. In this context, the application of wound dressings plays a pivotal role in facilitating tissue regeneration and minimizing infection risk. Modern wound dressings offer key advantages over traditional gauze by mimicking skin extracellular matrix (ECM) properties, maintaining moisture, and allowing oxygen flow. Unlike conventional dressings, they reduce pain, prevent epithelial damage, and eliminate the need for frequent changes, promoting faster and safer healing [3]. Sponge-based dressings are well-suited for full-thickness wounds, offering moisture retention and structural support while serving as carriers for therapeutic agents. Nanofibers, with their ECM-like architecture and high surface area, enhance cellular interactions [4]. By integrating these components, multilayered constructs such as sponge-nanofiber hybrids, more effectively replicate the hierarchical structure of native skin, providing synergistic benefits for advanced wound healing [5]. One of the most critical steps in designing an effective biomimetic wound dressing is the strategic selection of biomaterials that can reproduce the desired structural, biochemical, and functional properties required for optimal wound healing. Poly(allylamine hydrochloride) (PAH) is a synthetic, water-soluble, biodegradable cationic polymer characterized by a high density of amino groups, which exist either as free amines ($–NH_2$) or protonated ammonium salts ($+NH_3^+$) [6, 7]. Polyacrylic acid (PAA) is a water-soluble, non-toxic, and biodegradable anionic polymer characterized by a high density of carboxyl groups. Its strong hydrophilicity and superabsorbent properties make it an effective hydrogel-forming material for biomedical applications, particularly in moisture-retentive wound dressings [8,

10.57647/pibm.2025.1404.62

9]. PAH and PAA are two oppositely charged polyelectrolytes that readily dissolve in water. When mixed in aqueous solution, their cationic and anionic groups interact electrostatically to form stable polymeric complexes. This intrinsic ability to self-assemble without the need for external crosslinking agents stems from the reaction between the carboxyl groups of PAA and the amino groups of PAH, resulting in enhanced moisture resistance and mechanical integrity. Owing to their biocompatibility, these complexes have been widely explored in biomedical fields such as tissue engineering, drug delivery systems, and implant surface modification [10]. The ECM consists of structural polysaccharides and proteins that provide architectural support to surrounding tissues and regulate cellular adhesion, migration, and organization throughout the wound healing process [3]. Chitosan (Ch) is a linear polysaccharide derived from the alkaline N-deacetylation of chitin, composed of 2-amino-2-deoxy-D-glucopyranose units linked via 1,4-glycosidic bonds. Its low toxicity, biodegradability, and biocompatibility make it highly suitable for biomedical applications. Rich in amino and hydroxyl groups, Ch readily forms covalent bonds with various polymers and engages in electrostatic interactions with negatively charged molecules due to its cationic nature [11]. Fucoidan (Fc) is a sulfated polysaccharide primarily extracted from brown seaweeds, known for its ability to form gels and enhance integrin expression [12]. Its sulfate groups contribute to strong antibacterial, antioxidant, and immunomodulatory properties. Compared to other marine polysaccharides such as alginate, Fc demonstrates superior biological activity. Moreover, Fc effectively activates macrophages, suppressing the release of pro-inflammatory mediators and exerting notable anti-inflammatory effects [13]. Fc has been reported to interact with growth factors such as basic fibroblast growth factor (bFGF) and transforming growth factor-beta (TGF-β), enhancing their effects on cell proliferation, and mesenchymal stem cell activity by regulating their release and associated signaling pathways [14]. On the other hand, silk fibroin (SF) is a protein-based biopolymer with high strength, slow degradability, and excellent flexibility. Electrospun SF-based nanofibers closely mimic the ECM, supporting cell adhesion, proliferation, and migration [15, 16]. Localized drug delivery offers a targeted strategy for wound healing, overcoming poor perfusion in chronic wounds (such as diabetic wounds), improving local bioavailability, and minimizing systemic toxicity [17]. Sitagliptin (Sit) is a dipeptidyl peptidase-4 (DPP-IV) inhibitor widely used to regulate hyperglycemia in type 2 diabetes [18]. Beyond its glycemic control, Sit has shown therapeutic promise in promoting the healing of diabetic and ischemic wounds. It facilitates angiogenesis and enhances granulation tissue development, thereby accelerating the regenerative process in impaired wound environments [19, 20]. However, given Sit's limited bioavailability, short half-life, and rapid clearance, encapsulation within nanoparticles offers a compelling strategy to enhance therapeutic retention and optimize drug utilization [21, 22]. Furthermore, by leveraging their small size and targeting capabilities, nanoparticles improve pharmacokinetics, facilitate delivery to target cells, and enable sustained, site-specific release, ultimately enhancing therapeutic efficacy while minimizing systemic side effects [17, 23]. The aim of this study is to develop and evaluate a dual-layer biomimetic wound dressing tailored for diabetic wound healing, integrating both structural and biochemical functionalities. The upper layer consists of a PAA.PAH-based sponge matrix embedded with Fc-Ch nanoparticles loaded with Sit, and the lower layer comprises electrospun nanofibers made of SF. The novelty of the present study lies in the rationally designed dual-layer architecture with clearly separated yet synergistic functionalities. The upper polyelectrolyte sponge layer serves as a highly absorbent matrix and a sustained drug delivery platform through sitagliptin-loaded fucoidan–chitosan nanoparticles, while the lower electrospun SF nanofibrous layer specifically mimics the ECM to promote early cell adhesion and spreading. This hierarchical integration enables simultaneous control of wound exudate, localized drug release, and cell–material interactions, resulting in synergistic wound management and healing effects. In contrast to previously reported single-layer dressings or sponge–nanofiber systems, the present dressing uniquely integrates bioactive polysaccharide-based nanoparticles within a superabsorbent polyelectrolyte sponge matrix, while simultaneously incorporating a protein-based electrospun nanofibrous layer to enhance chemical and structural similarity to the ECM. To the best of our knowledge, this specific combination of material composition and hierarchical architecture has not been demonstrated in earlier wound dressing designs. Comprehensive physicochemical, mechanical, and biological characterizations were performed, and the wound healing efficacy was validated in a diabetic rat model.

2. Materials and methods

2.1. Materials

Poly(allylamine hydrochloride) (PAH, ~17.5 kDa), polyacrylic acid (PAA, ~450 kDa), and chitosan (medium molecular weight, 75–85% deacetylated) were

obtained from Sigma-Aldrich (USA), together with dimethyl sulfoxide (DMSO), fucoidan (≥85% purity), and dimethyl thiazole diphenyltetrazolium bromide (MTT). Sitagliptin (Sit) powder was supplied by Sanamed-Pharma (Iran). Silk fibroin (SF, ~100 kDa), extracted from *Bombyx mori* cocoons, was provided by Medisa Polymer Aria (Iran). Dulbecco's modified Eagle's medium (DMEM) was purchased from Vivacell (USA). Injectable ketamine (Rotexmedica, Germany) and xylazine (Alfasan, Netherlands) were also procured for experimental use.

2.2. Synthesis and characterization of Sit-loaded Fc-Ch nanoparticles

The nanoparticles were prepared using a polyelectrolyte self-assembly approach [24, 25], which relies on the electrostatic attraction between negatively charged Fc and positively charged Ch. To begin, Ch was dissolved in 1% acetic acid to obtain a 1 mg/mL solution, while Fc was dissolved in distilled water at a concentration of 5 mg/mL. The two solutions were then mixed at a Fc-to-Ch powder ratio of 5:1. The mixture was subjected to pulse sonication at full amplitude (3 seconds on and 3 seconds off) for a total of 30 seconds to promote the controlled formation of nanoparticles. Larger aggregates were removed using an 800 nm syringe filter, and the nanoparticles were subsequently collected by centrifugation and then freeze-dried. To improve the nanoparticle yield, the pulse sonication and subsequent separation steps were repeated five times before the final collection and freeze-drying. Additionally, to obtain Sit-loaded nanoparticles, Sit powder (1.5 mg/mL) was first dissolved in the mixed solution [26], followed by the same sonication, purification and lyophilization steps as described above. Finally, the encapsulation efficiency and drug loading capacity were determined according to Equations 1 and 2, respectively.

$$\text{Encapsulation efficiency } (\%) = \frac{\textit{Initial Sit added} - \textit{Free Sit in the supernatant}}{\textit{Initial Sit added}} \times 100$$

Equation 1

$$\textit{Encapsulation capacity } (\%) = \frac{\textit{Mass of encapsulated Sit}}{\textit{Totall mass of Nanoparticles}} \times 100$$

Equation 2

To assess the particle size and morphological features, a droplet of nanoparticle suspension (0.1 mg/mL) was placed onto a carbon-coated copper grid and left to air dry. The dried specimens were subsequently visualized using transmission electron microscopy (TEM; PHILIPS EM208S) operated at an accelerating voltage of 100 kV. The resulting micrographs were processed and quantitatively analyzed using ImageJ software.

Furthermore, dynamic light scattering (DLS; Cordouan Technologies, France) was utilized to evaluate the particle size, polydispersity index (PDI), and zeta potential of the synthesized nanoparticles.

2.3. Preparation of wound dressings

To fabricate the sponge-like wound dressings, as well as the sponge layer of the dual-layer construct, an aqueous solution of 10% w/v polyacrylic acid (PAA) was first prepared and stirred for 1 hour. Subsequently, 8% w/v polyallylamine hydrochloride (PAH) was added to the solution, followed by vigorous stirring at room temperature for an additional hour to ensure homogeneity. Accordingly, the PAA.PAH solution was successfully prepared. To formulate the nanoparticle-containing mixtures, Fc-Ch nanoparticles and Sit-loaded Fc-Ch nanoparticles were separately added to the PAA.PAH solution at a concentration of 20 mg/mL [27], yielding PAA.PAH.NPs and PAA.PAH.SitNPs formulations, respectively. Finally, to generate porous sponge-like structures, 0.5 mL of each formulation was dispensed into the wells of a 24-well culture plate. The samples were frozen at −20 °C and subsequently subjected to lyophilization. The resulting sponges derived from PAA.PAH, PAA.PAH.NPs, and PAA.PAH.SitNPs solutions were designated as Spg1, Spg2, and Spg3, respectively.

For the fabrication of the Dual-layer dressing, the electrospinning solution was first prepared. For this purpose, a 14% (w/v) solution of SF in formic acid was prepared and stirred for 2 hours [28, 29]. For electrospinning, the Spg3 specimen was fixed on the collector at a distance of 15 cm from the needle tip. The solution prepared earlier was loaded into a 5 mL syringe fitted with 0.4 mm inner-diameter needle, and the process was carried out under a voltage of 20 kV with a flow rate of 0.5 mL/h, leading to the formation of the Dual-layer dressing. Following electrospinning, methanol was sprayed onto the nanofiber mat, and the samples were subsequently dried for 24 hours.

2.4. Characterization

The surface features of the wound dressings, along with the cross-sectional morphology of the Dual-layer construct, were examined using a scanning electron microscope (SEM; LEO435VP, UK) after sputter-coating with gold, at an accelerating voltage of 18.00 kV. Quantitative analysis of the internal architecture was performed by measuring both the pore dimensions of the sponge matrices and the fiber

diameters within the nanofibrous layer. For each sample, twenty independent measurements (n = 20) were obtained using ImageJ software, and the resulting data were expressed as mean values. The functional groups of the components and their possible interactions in the samples were analyzed using FT-IR spectroscopy (6300, JASCO, Japan). Spectra were recorded within the 600–4000 cm^{-1} region at a resolution of 4 cm^{-1}. To evaluate water uptake and hydration performance, both the sponges and the Dual-layer construct were subjected to swelling tests in distilled water. Their initial dry mass (Wi) was recorded, followed by immersion at 37 °C for defined intervals. After blotting away excess moisture with filter paper, the wet mass (Ww) was determined, and the swelling ratio was calculated according to Equation 3:

$$Swelling\ (\%) = \frac{Ww-Wi}{Wi} \times 100$$

Equation 3

2.5. *In vitro* degradation

Biodegradability of the dressings was assessed following ASTM F1635–11. Initially, the specimens were recorded in their dry state (Wi) and subsequently incubated in vials containing 10 mL of phosphate-buffered saline (PBS) at 37 °C. At predetermined intervals (1, 3, 5, and 7 days), the samples were withdrawn, freeze-dried to remove residual moisture, and reweighed (Wt). The degradation rate was then calculated according to Equation 4 [30]:

$$Degradation\ (\%) = \frac{Wi-Wt}{Wi} \times 100$$

Equation 4

where Wi represents the initial dry weight of the samples prior to degradation, and Wt denotes the weight measured after degradation.

2.6. Evaluation of Sit release

Release profiles of Sit from both the Spg3 and Dual-layer dressing were investigated in PBS. Specimens were incubated in 50 mL PBS at 37 °C, and aliquots of 3 mL were withdrawn and replaced with fresh medium at predetermined intervals (1, 3, 5, and 7 days). The collected solutions were analyzed by UV–Vis spectrophotometry at 267 nm to quantify Sit concentration [26]. Cumulative release profiles were subsequently calculated and plotted, based on triplicate measurements (n = 3) for each formulation.

2.6.1. *Release kinetics*

The release kinetics of Sit from the Spg3 and Dual-layer wound dressings were investigated using Equations 5–8, based on zero-order, first-order, Higuchi, and Korsmeyer–Peppas models [31, 32]:

Zero-order: $$Q_t = Q_0 + K_o t$$

Equation 5

First-order: $$log\, Q_t = log\, Q_0 - \frac{K_1 t}{2.303}$$

Equation 6

Higuchi: $$Q_t = K_H t^{0.5}$$

Equation 7

Korsmeyer–Peppas: $$log\ (\frac{Q_t}{Q_\infty}) = n\ log\ t\ +\ log\ k$$

Equation 8

where Q_t is the amount of drug released at time t, and Q_0 is the initial amount of drug in the wound dressings. K_0, K_1, and K_H represent the zero-order constant, the first-order constant, and the Higuchi dissolution constant, respectively. In the Korsmeyer–Peppas release model, "*k*" is the kinetic constant and "*n*" is the release exponent that explains the release mechanism.

2.7. Tensile properties

Mechanical performance of the wound dressings was assessed by tensile testing using a universal testing machine (Hounsfield H25KS, UK) in accordance with ASTM D-882. Rectangular specimens (30 × 10 mm) were hydrated in PBS prior to testing, mounted on the grips, and subjected to uniaxial extension at a constant crosshead speed of 1 mm/min until rupture [33]. Tensile properties were determined from the recorded stress-strain curve, with each experiment conducted in triplicate (n = 3).

2.8. Cytocompatibility

Cytocompatibility of the wound dressings was examined using L929 fibroblast cells sourced from the Pasteur Institute Cell Bank (Iran). Cells were cultured in DMEM supplemented with 10% fetal bovine serum (FBS) under standard conditions of 37 °C, 5% CO_2, and 95% relative humidity. Prior to experimentation, cells were enzymatically detached with trypsin, resuspended in PBS, and prepared for seeding. Dressing specimens were sterilized by ultraviolet irradiation for 20 min on each side, rinsed with DMEM, and positioned in 24‑well culture plates. A suspension containing 2×10^4 cells was seeded onto each sample and incubated for 1 and 7 days. At the specified time points, the medium was replaced with fresh DMEM containing 0.5 mL MTT solution, followed by a 4-hour incubation to enable mitochondrial reduction of MTT into formazan crystals. After incubation, the medium was discarded, crystals were solubilized in 0.5 mL of DMSO, and 0.1 mL of each solution was transferred to a 96‑well plate. Optical

density was measured at 570 nm using an ELISA reader to determine cell viability. Wells without dressings served as controls (n = 3). Morphological features and adhesion behavior of L929 fibroblasts on the wound dressings were investigated by SEM. A suspension containing 2×10^4 cells was seeded onto each specimen and cultured for 24 hours under standard conditions. Following incubation, cells were chemically fixed with 3.5% glutaraldehyde at 4 °C. The samples were then dehydrated through a graded ethanol series (50%, 60%, 70%, 80%, and 99%), with each step lasting 15 minutes. After preparation, the specimens were subjected to SEM observation to visualize cell attachment and morphology.

2.9. *In vivo* wound healing

All animal experiments were performed in compliance with the European Union Directive 2010/63/EU and under the supervision of a certified animal care specialist. Male Wistar rats, approximately 4 months old and weighing around 300 g, were selected for the study. Prior to intervention, animals were acclimatized for one week under controlled environmental conditions, including a 12 h light/dark cycle, ambient temperature of 25 °C, and unrestricted access to water and standard chow. A total of 30 rats were randomly allocated into five experimental groups: Control, Spg1, Spg2, Spg3, and Dual‑layer. To establish the diabetic model, rats received a single intraperitoneal dose of streptozotocin (60 mg/kg), prepared freshly in 0.1 M citrate buffer at pH 4.5. After induction, fasting blood glucose was monitored daily with a glucometer for one week. Animals that consistently displayed glucose concentrations of 300 mg/dL or higher in two successive assessments were identified as diabetic and subsequently included in the *in vivo* experiments [34]. Rats designated for surgery were first anesthetized with ketamine (80 mg/kg) combined with xylazine (10 mg/kg). After shaving the dorsal region, the operative site was sterilized using 70% ethanol followed by betadine. A 1 cm^2 circular, full‑thickness excision wound was produced with a punch biopsy instrument. In treatment groups, the wounds were immediately covered with dressings (except control), and the dressings were renewed on day 7. Wound sites were photographed macroscopically on days 1, 7, and 14 to determine the closure rate. At the end of the 14‑day period, animals were sacrificed via carbon dioxide inhalation. The wound specimens were harvested, immersed in 10% formalin for fixation, sectioned at 4 µm thickness, and subsequently stained with hematoxylin and eosin (H&E) as well as Masson's trichrome for histological evaluation. To characterize gene expression during the early phase of wound repair, quantitative real-time PCR (qRT-PCR) analysis was conducted on day 7 following treatment. The transcriptional levels of vascular endothelial growth factor (VEGF), transforming growth factor-β (TGF-β), tumor necrosis factor-α (TNF-α), and interleukin-1β (IL-1β) were determined. For molecular evaluation, three rats from each group were sacrificed on day 7, and wound tissues were collected. Total RNA was isolated from homogenized samples using TRIzol reagent according to the manufacturer's instructions. The yield and purity of RNA were assessed spectrophotometrically with a NanoDrop 2000 device (Thermo Scientific, USA). Complementary DNA (cDNA) was then synthesized from the extracted RNA employing the iScript™ cDNA Synthesis Kit (Bio-Rad). Amplification of target transcripts was performed on a Bio-Rad real-time PCR system. Each reaction was run in triplicate to ensure reproducibility of the data. Glyceraldehyde-3-phosphate dehydrogenase (GAPDH) was used as the internal reference gene to normalize expression values. All primer sequences used in the qRT‑PCR assays are listed in Table 1 [35].

2.10. Statistical analysis

All statistical analyses were performed using GraphPad Prism (v8.0). Differences among groups were evaluated by one-way analysis of variance (ANOVA). When overall significance was observed, Tukey's post-hoc test was applied to determine pairwise group differences. Data are expressed as mean values accompanied by standard deviation. A p-value below 0.05 was considered statistically significant. Levels of significance were indicated as follows: * for $p < 0.05$, ** for $p < 0.01$, *** for $p < 0.001$, and **** for $p < 0.0001$.

Table 1. Primer sequences applied for quantitative qRT‑PCR gene expression analysis

Gene	Forward Primer	Reverse Primer
VEGF	AGGCTGCACCCACGACAGAA	CTTTGGTCTGCATTCACATC
TGF-β	CATTGCTGTCCCGTGCAGA	AGGTAACGCCAGGAATTGTTGCTA
IL-1β	TCTGAAGCAGCTATGGCAAC	TCAGCCTCAAAGAACAGGTCA
TNF-α	GCTCCCTCTCATCAGTTCCA	GCTTGGTGGTTTGCTACGAC
GAPDH	CAGCAATGCATCCTGCAC	GAGTTGCTGTTGAAGTCACAGG

3. Results and discussion

Chronic diabetic wounds demand advanced therapeutic strategies that can actively support the healing process. To address this need, a dual-layer biomimetic wound dressing was constructed, combining a PAA.PAH sponge matrix embedded with Fc–Ch nanoparticles loaded with Sit and an electrospun SF nanofibrous layer. This Dual-layer dressing was further compared with three sponge-based counterparts (Spg1, Spg2, and Spg3) in terms of physicochemical, mechanical, and biological properties.

3.1. Morphological characterization

As shown in the TEM images in Figure 1, the morphology of the synthesized nanoparticles, reveals irregular and non-uniform structures with no defined geometric shape. Despite their disordered appearance, both Fc–Ch and Sit-loaded Fc–Ch nanoparticles remain within the nanoscale range, with average diameters of approximately 208.4 ± 40.2 nm and 214.8 ± 74.7 nm, respectively. No significant differences in size or overall morphology could be distinguished between Fc–Ch nanoparticles and their Sit-loaded counterparts, indicating that drug incorporation did not markedly alter the structural characteristics of the nanoparticles. The irregular morphology of the nanoparticles can be attributed to the freeze-drying step at the end of the synthesis process, during which ice crystal formation and drying-induced stresses can lead to surface wrinkling, partial aggregation, and structural heterogeneity. While lyophilization is essential for long-term stabilization and storage, it often introduces morphological distortions that affect the final appearance of polymer-based nanoparticles [36, 37]. Moreover, DLS analysis was employed to evaluate the hydrodynamic size, PDI, and surface charge (zeta potential) of the synthesized nanoparticles (Table 2). The results revealed that Fc–Ch nanoparticles had an average diameter of 423.19 nm and a PDI of 0.17. Upon Sit encapsulation, the hydrodynamic diameter increased to 497.30 nm, consistent with drug incorporation, while the PDI slightly decreased to 0.16. The variation in particle size between TEM and DLS measurements arises from methodological differences. TEM captures images of a restricted subset of particles, whereas DLS provides a statistical average over the entire suspension. Moreover, DLS calculations assume spherical particles with a hydrodynamic solvent layer, while TEM clearly indicated deviations from perfect sphericity [38]. Both nanoparticle formulations exhibited negative zeta potential values (−44.4 mV for Fc–Ch and −42.2 mV for Sit-loaded Fc–Ch), suggesting electrostatic repulsion between particles and indicating good colloidal stability. The observed negative surface charge is likely associated with the higher proportion of Fc in the nanoparticles, owing to the sulfate groups present along its backbone. These observations are consistent with results reported in previous studies [39, 40].

Overall, the synthesized nanoparticles remain within the standard nanoscale range (20–500 nm) reported for wound-healing applications [41], and can therefore be considered well-suited as drug-delivery carriers in diabetic wound therapy. The morphology and microstructure of the sponge dressings (Spg1, Spg2, and Spg3) and Dual-layer dressing, as examined by SEM imaging, are presented in Figure 2. All three sponges exhibited highly porous architectures with interconnected pores and irregular surface topographies (Figure 2a). The average pore diameters were measured to be 242.7 ± 47.6 µm for the Spg1, 200.3 ± 39.5 µm for the Spg2, and 193.2 ± 38.9 µm for the Spg3. The reduced pore size observed in the Spg2 and Spg3 formulations compared to the Spg1, can be attributed to the presence of nanoparticles in the precursor solution, which increased the overall concentration and viscosity prior to freeze-drying, leading to a more compact and organized pore architecture [42]. The open-pore networks observed across all sponge samples are favorable for exudate absorption, nutrient diffusion, and cellular infiltration, which are key parameters for effective wound healing [43, 44]. Figure 2b shows the electrospun SF nanofibers served as the bottom layer in the Dual-layer wound dressing. The nanofibers exhibited a continuous, bead-free morphology with random orientation and dense packing, indicating well-controlled fabrication. The average fiber diameter was measured at 485.50 ± 50.02 nm, which is suitable for mimicking ECM features and facilitating cellular interactions. Figure 2c presents a cross-sectional SEM image of the Dual-layer dressing, clearly demonstrating the integration between the SF nanofibrous layer and the sponge matrix. The thickness of the sponge layer was measured about 953.60 ± 34.08 µm, while the thickness of the nanofibrous layer was determined to be 776.42 ± 49.27 µm. The fibrous layer is uniformly anchored to the sponge, with appropriate physical interlocking and no signs of delamination. The engineered Dual-layer wound dressing was designed to integrate two complementary structural components, each serving distinct biological functions. The SF nanofibrous layer, positioned at the base of the construct, can mimic the architecture of native ECM by providing a high surface area and nanoscale topography that promotes initial cell adhesion, spreading, and signaling. On the other hand, the overlying sponge layer

contributes additional functionality by offering a porous, volumetric structure capable of absorbing wound exudate while simultaneously enabling cell infiltration, migration, capillary ingrowth and angiogenesis. In fact, the coexistence of multiple pore size scales—nanometric in the fibrous layer and micrometric in the sponge—creates a dual-porosity environment that supports both surface-level cell anchorage and deeper tissue integration [45, 46].

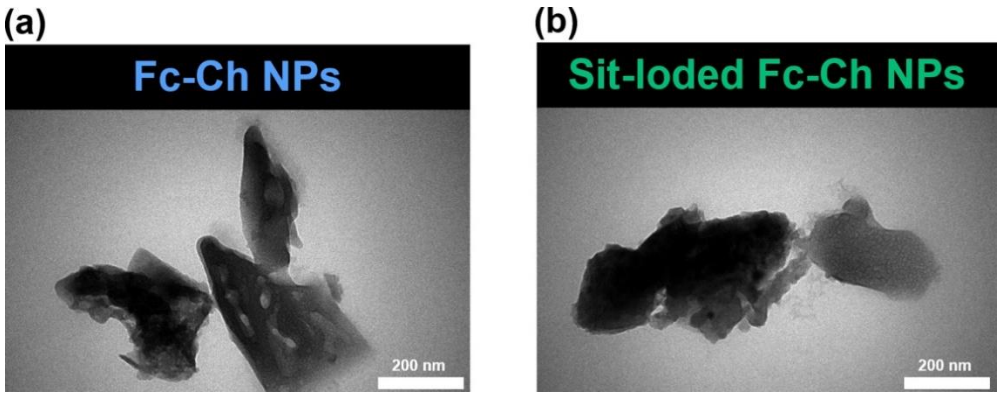

Figure 1. TEM images of (a) Fc–Ch nanoparticles and (b) Sit-loaded Fc–Ch nanoparticles

Table 2. Characteristics of synthesized nanoparticles measured by DLS

Nanoparticle sample	Z-average (nm)	PDI	Zeta potential (mV)
Fc-Ch	423.19	0.17	-44.4
Sit-loaded Fc-Ch	497.30	0.16	-42.2

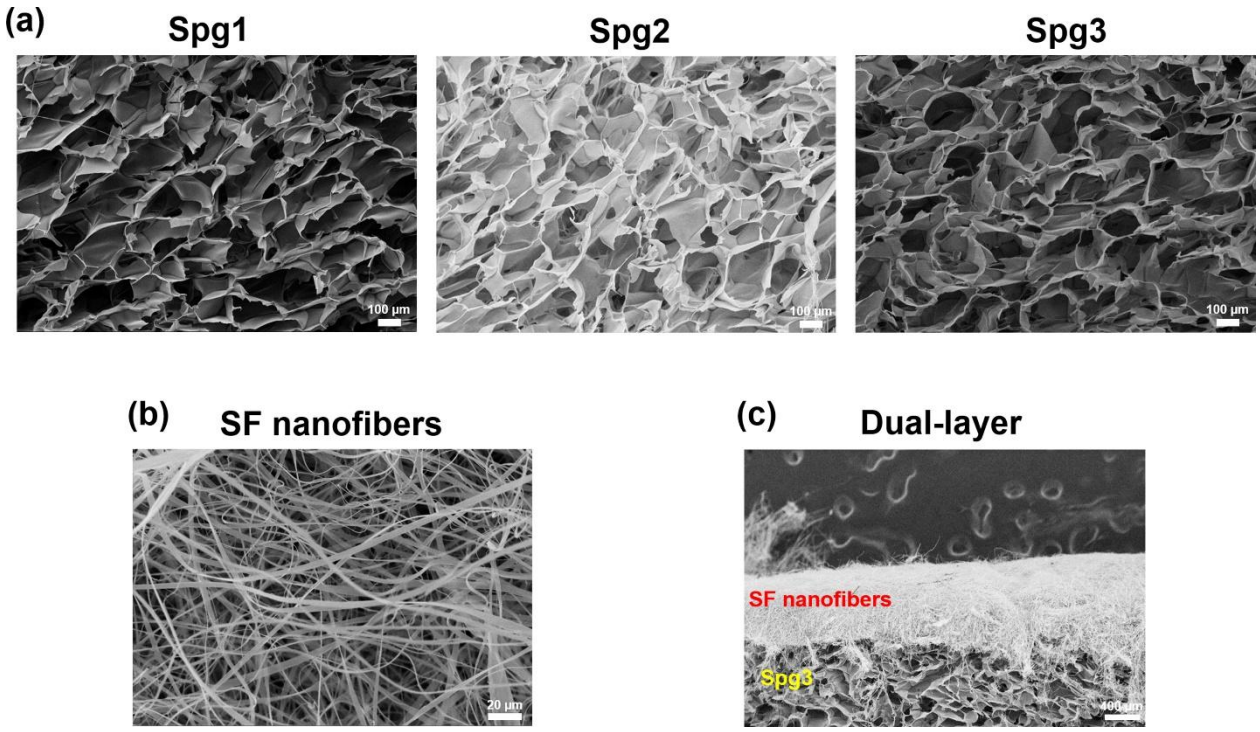

Figure 2. SEM micrographs showing (a) the porous morphology of the Spg1, Spg2, and Spg3 wound dressings, (b) the fibrous structure of the SF nanofibers, and (c) the cross-sectional architecture of the Dual-layer wound dressing

10.57647/pibm.2025.1404.62

3.2. Chemical investigation

To elucidate the chemical structure and confirm the presence of different constituents within the fabricated wound dressings, FTIR analysis was performed, and the resulting spectra are displayed in Figure 3. In the spectrum of the Spg1, the appearance of strong peaks in the 2600–3000 cm^{-1} region corresponds to the stretching mode of the $–NH_3^+$ group in PAH, which overlaps with the bands associated with CH_2 asymmetric and symmetric stretching modes. Additionally, the peaks observed at 1471 and 1100 cm^{-1} are attributed to the bending vibrations of the $–NH_3^+$ group and the C–N stretching vibrations in amines, respectively [47]. The broad band observed around 3500 cm^{-1} and the band at 1727 cm^{-1} correspond to the OH stretching vibration and the C=O stretching of PAA, respectively [8]. Upon interaction with the protonated ammonium groups of PAH, these bands exhibit weak intensities. Furthermore, the presence of an N–H band around 1700 cm^{-1} together with the unusually low frequency of the C=O stretching suggests the formation of amide groups, whereby the C=O band partially overlaps with the N–H bending vibration in the 1700–1730 cm^{-1} region and consequently appears as a doublet [48]. Therefore, it can be concluded that the polyelectrolyte complex between PAH and PAA was successfully formed. In the FTIR spectrum of Sit-loaded Fc-Ch nanoparticles, the absorption band at 850 cm^{-1} corresponds to the β-1,4 glycosidic linkage of the Ch backbone, the peak at 1016 cm^{-1} is attributed to C–O stretching vibrations of primary and secondary alcohol groups, and the band at 1150 cm^{-1} arises from C–O–C stretching vibrations of glycosidic bonds within the polysaccharide structure. Also, the band appeared at 1653 cm^{-1} corresponds to Amide I (C=O stretching), while the band at 1523 cm^{-1} is related to Amide II (N–H bending and C–N stretching). The broad band observed in the region of 3500–3600 cm^{-1} is attributed to the overlapping stretching vibrations of hydroxyl (O–H) groups and amino (N–H) groups [49]. The absorption bands corresponding to the saccharide structures of Fc overlap with those of Ch, while the stretching vibrations of the sulfonate group in Fc are distinctly evidenced by a characteristic peak at 1271 cm^{-1} [50]. Although most of the characteristic peaks of Sit overlap with those of Ch and Fc, the presence of Sit within the nanoparticles can be confirmed by the distinct band at 1722 cm^{-1}, which corresponds to the C=O group [21]. The FTIR spectrum of the Spg3 exhibits all the characteristic peaks of its individual components; however, the incorporation of Sit-loaded Fc-Ch nanoparticles leads to the overlap of their characteristic bands within the 1700–1730 cm^{-1} region, resulting in a modest increase in intensity and slight broadening of the peak in this area compared to the Spg1. In the FTIR spectrum of the Dual-layer sample, all the characteristic peaks of the constituent components are detectable with altered intensities due to the extensive hydrogen bonding among them; however, the presence of the nanofibrous SF layer, and the overlap of Amide I and Amide II bands with the characteristic peaks of other components, resulted in an increase in intensity and slight broadening of the peaks observed in the 1523–1730 cm^{-1} region [51].

3.3. Swelling, degradation and drug release

High water absorption and swelling capacity without structural disintegration are essential features of a modern wound dressing, enabling efficient exudate management while maintaining a moist wound environment conducive to healing. The swelling profiles of Spg1, Spg2, Spg3, and Dual-layer dressings were monitored over 72 hours in distilled water, as shown in Figure 4a. All samples exhibited a rapid increase in swelling during the initial 36-48 hours, followed by a plateau or slight decline until 72 hours. The equilibrium swelling ratios of the Spg1, Spg2, Spg3, and Dual-layer samples were measured to be 383.3 ± 20.7%, 464.3 ± 26.6%, 477.8 ± 43.0%, and 512.2 ± 21.9%, respectively. The significantly higher swelling observed in the Spg2 and Spg3 compared to the Spg1 ($p < 0.05$) can be attributed to the presence of Fc–Ch-based nanoparticles within the sponge matrix. Due to the abundance of amino and hydroxyl groups, Fc–Ch nanoparticles can interfere with the polyelectrolyte network by competing with interpolymeric interactions, which disrupts network cohesion and increases free volume, thereby enhancing water uptake in nanoparticle-containing sponges [52]. Also, the Dual-layer dressing demonstrated a higher swelling capacity compared to the Spg2 and Spg3 ($p < 0.05$), primarily due to the presence of an additional hydrophilic nanofibrous layer with a high specific surface area. The biodegradation behavior of the fabricated sponge-based and the Dual-layer wound dressings was evaluated by monitoring their weight loss in PBS over a 7-day period. As shown in Figure 4b, all samples exhibited a time-dependent increase in weight loss, reflecting their progressive degradation. Following 7 days of incubation, the Spg1 showed a weight loss of 25.5 ± 2.6%, whereas the Spg2, Spg3, and the Dual-layer dressings showed significantly higher degradation, with values ranging between 36.0 and 38.2% ($p < 0.05$). Consistent with the trends observed in water uptake and swelling behavior, the nanoparticle-containing dressings exhibited higher biodegradability in 7 days. Therefore, water absorption and the hydrolytic degradation of the

dressing components are considered the primary contributors to the observed weight loss in PBS. Overall, the observed degradation profiles suggest that the dressings were tunable in terms of biodegradability, suitable for wound environments requiring gradual material resorption, sustained release of therapeutic agents, and progressive replacement by newly regenerated tissue. The release behavior of Sit from the Spg3 and Dual-layer wound dressings was assessed over a 7-day period. As illustrated in Figure 4c, both systems demonstrated a progressive, time-dependent increase in cumulative Sit release, with the Spg3 consistently yielding higher levels at all measured intervals. After 7 days, the cumulative release of Sit from the Spg3 and Dual-layer dressings was measured at 89.3 ± 9.3% and 82.4 ± 6.2%, respectively. Although the Dual-layer construct showed a slightly lower release, the difference between the two formulations was statistically insignificant ($p > 0.05$). The presence of an electrospun nanofibrous layer in the Dual-layer system likely contributed to a more controlled release behavior, acting as a diffusion barrier that modulates drug transport from the sponge matrix into the surrounding medium. Swelling, diffusion and degradation of the dressings served as key triggers for Sit release, facilitating gradual diffusion into the surrounding medium. Such drug delivery systems, like the designated wound dressings, can sustain therapeutic agent release while maintaining drug concentrations within the therapeutic window and reducing systemic side effects [53, 54].

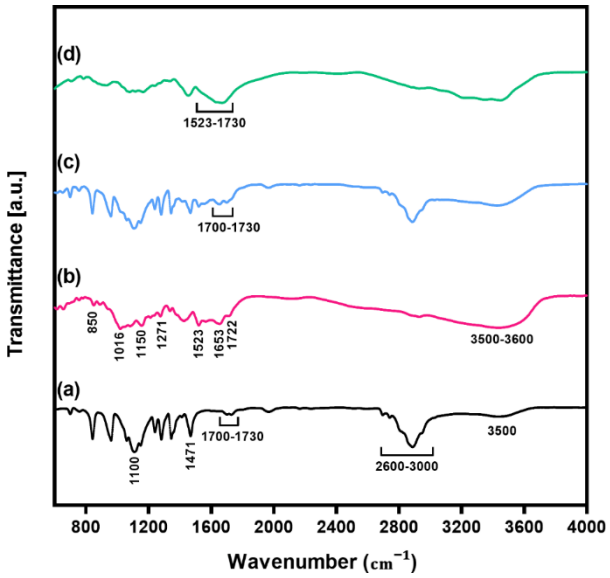

Figure 3. FTIR spectra of (a) Spg1 composed of PAA.PAH, (b) Sit-loaded Fc–Ch nanoparticles, (c) Spg3 composed of PAA.PAH containing Sit-loaded nanoparticles, and (d) the Dual-layer dressing

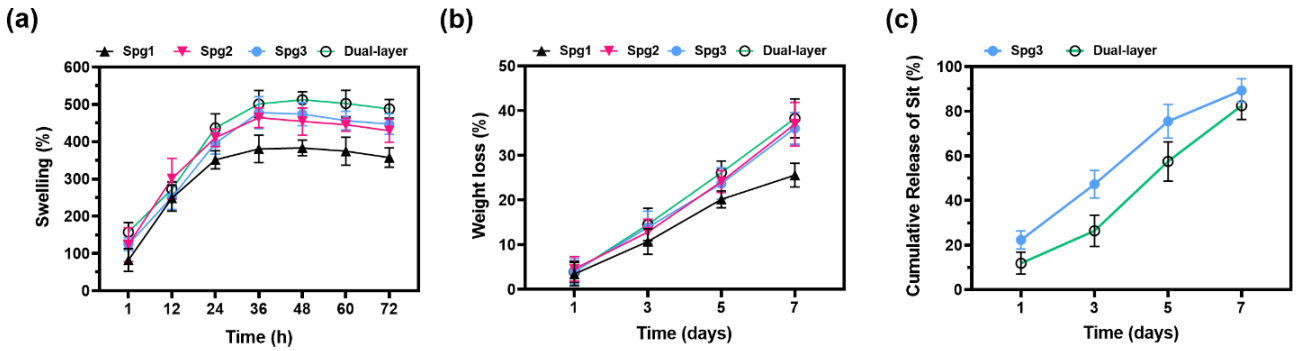

Figure 4. (a) Swelling behavior of the fabricated wound dressings in distilled water during 72 hours, (b) biodegradation profiles in PBS over a 7‑day incubation period, and (c) cumulative release of Sit from Spg3 and Dual‑layer dressings over 7 days

To better understand the drug release mechanism from the Spg3 and Dual-layer dressings, the release data were fitted to various kinetic models, including Zero-order, First-order, Higuchi, and Korsmeyer–Peppas, and the results are summarized in Table 3. For the Spg3 dressing, the Korsmeyer–Peppas model provided the best fit with a correlation coefficient of $R^2 = 0.9955$. The release exponent (n = 0.7293) for this wound dressing suggests an anomalous transport mechanism, reflecting a combination of drug diffusion and polymer chain swelling/relaxation [55]. This behavior is consistent with the porous sponge-like structure and high-water absorption capacity of the Spg3 scaffold. In contrast, the Dual-layer dressing showed the highest fit with the Zero-order model ($R^2 = 0.9867$) and an acceptable fit with the Korsmeyer–Peppas model ($R^2 = 0.972$). The release exponent for this scaffold ($n \approx 1$) indicates a Case II transport mechanism, which is typically associated with Zero-order release, where polymer swelling and chain relaxation predominantly govern drug release while diffusion plays a minor role [55]. This behavior can be attributed to the dual-layer structure of the dressing, in which the nanofibrous layer acts as a barrier, preventing excessive drug diffusion and ensuring sustained and controlled release.

3.4. Tensile properties

The tensile strength of a dressing is a key determinant of its capacity to withstand handling stresses and maintain effective mechanical protection of the wound [56]. Since diabetic wounds are generally associated with considerable exudate, the mechanical performance of dressings under wet conditions becomes particularly important. Therefore, the tensile properties of the dressings were evaluated in the hydrated state and are depicted in Figure 5. As evident, the tensile strength, elastic modulus, and elongation of the dressings were measured in the ranges of 170–354 KPa, 417–987 KPa, and 110–171%, respectively. The lower limits of these ranges correspond to the Spg1 dressing, while the upper limits are associated with the Dual-layer dressing. Statistical analysis revealed no significant variation in the tensile properties of the sponge dressings (Spg1, Spg2, and Spg3) ($p > 0.05$); however, the Dual-layer dressing demonstrated a marked enhancement in tensile behavior ($p < 0.01$). This improvement in tensile properties is directly attributed to the presence of SF nanofibers. SF nanofibers act as a reinforcing network, enhancing load transfer and mechanical stability. SF consists of β-sheet crystallites and amorphous domains, where the crystalline regions provide strength and the amorphous segments enable extensibility. The β-sheet crystalline domains of SF nanofibers primarily contribute to tensile strength and stiffness, while indirectly supporting elasticity by anchoring amorphous regions that undergo reversible deformation [57], which synergistically improve the overall mechanical performance of the Dual-layer dressing compared to the sponge dressings. Mohandas et al. [58] developed drug-loaded bi-layered sponges composed of hyaluronic acid and chitosan for wound management under hyperfibrinolytic conditions, reporting tensile strength values of about 0.08–0.1 MPa and elongation of about 35–45%. They concluded that these values were adequate for wound dressing applications. Furthermore, previous related studies have also reported tensile properties comparable to those obtained in the present work [33, 59, 60], confirming that both the sponges and Dual-layer dressings fabricated herein possess mechanically acceptable characteristics for wound healing applications.

Table 3. Comparison of kinetic models for Sit release from wound dressings, showing correlation coefficients (R^2) and the Korsmeyer–Peppas release exponent (n)

Samples	Kinetic models (7 days)				
	Zero-order	First-order	Higuchi	Korsmeyer-Peppas	
	R^2	R^2	R^2	R^2	n
Spg3	0.9768	0.9774	0.977	0.9955	0.7293
Dual-layer	0.9867	0.9142	0.9625	0.9723	1.0006

10.57647/pibm.2025.1404.62

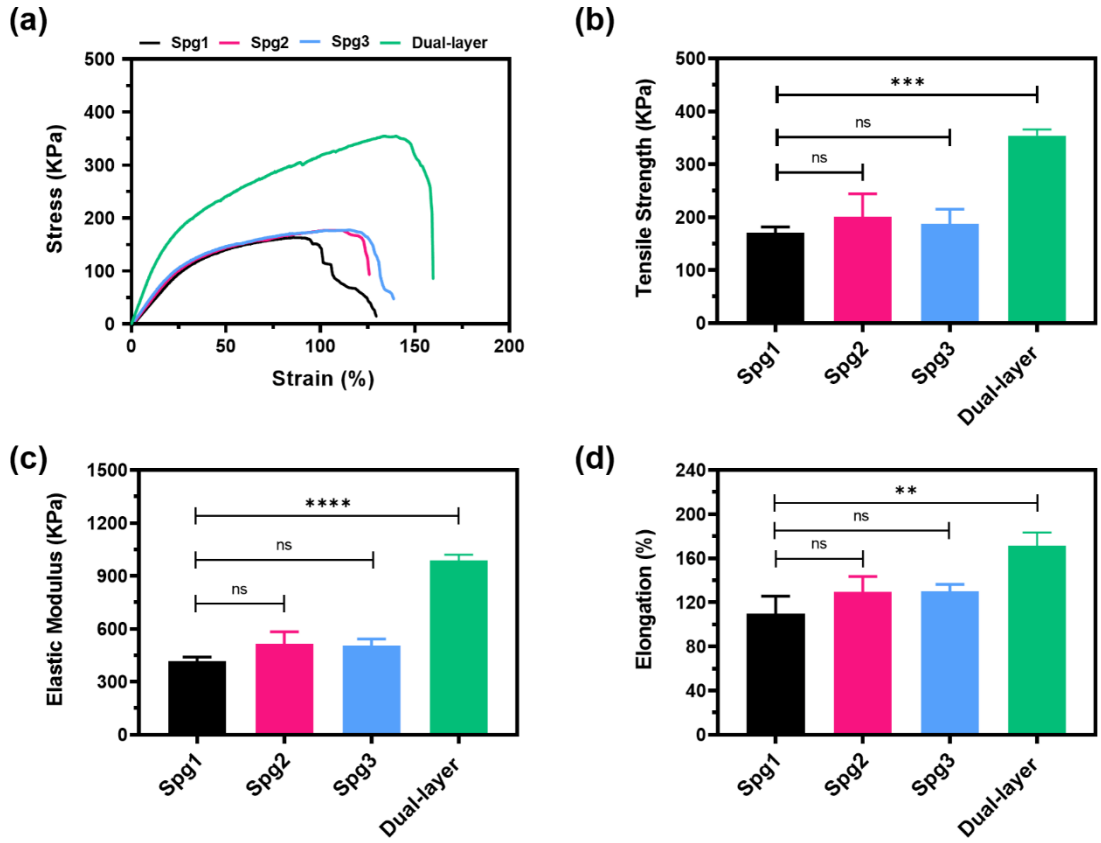

Figure 5. Tensile properties of the fabricated wound dressings: (a) representative stress–strain curves, and bar charts of: (b) tensile strength, (c) elastic modulus, and (d) elongation at break. Significant differences are marked as "ns: not significant, **: $p < 0.01$, ***: $p < 0.001$, and ****: $p < 0.0001$"

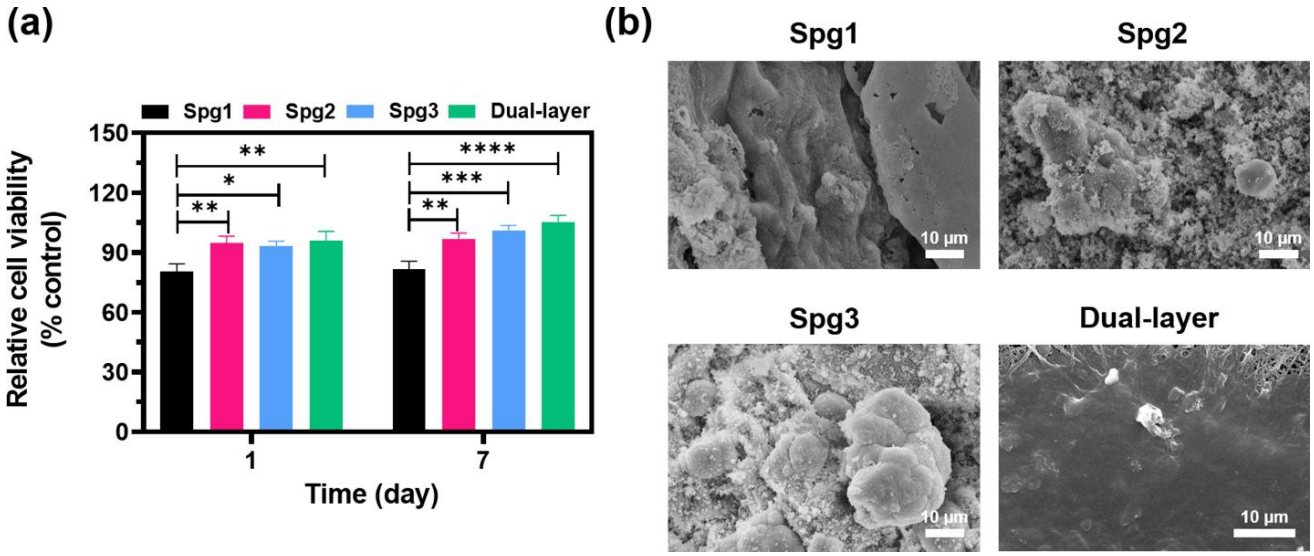

Figure 6. (a) MTT assay results showing the viability of L929 fibroblasts cultured on different wound dressings at 1 and 7 days. (b) representative SEM micrographs illustrating cell morphology and adhesion behavior after 24 hours of culture. Significant differences are marked as "*: $p < 0.05$, **: $p < 0.01$, ***: $p < 0.001$, and ****: $p < 0.0001$"

3.5.Cytocompatibility

To explore the biological performance of the fabricated wound dressings, their cytocompatibility was examined through MTT assay alongside the observation of L929 fibroblast adhesion and spreading on the dressing surfaces, providing insight into their potential for supporting cellular activity during wound healing. Figure 6a illustrates the cell viability of L929 fibroblasts cultured on different wound dressings, as determined by MTT assay at days 1 and 7. The nanoparticle-containing wound dressings exhibited higher cell viability than the Spg1 dressing at both day 1 and day 7. At day 1, the Spg3 dressing exhibited lower cell viability compared to Spg2 and the Dual-layer construct. This reduction can be attributed to the faster release of Sit from the Spg3 relative to the Dual-layer dressing, which likely has exerted a negative influence on cellular viability. Previous studies have also highlighted the ability of Sit to attenuate the proliferation of different fibroblast types [18, 61]. Conversely, dressings containing Sit-loaded nanoparticles (Spg3 and Dual-layer) demonstrated higher cell viability than Spg2 at day 7 ($p < 0.05$), with the Dual-layer construct exhibiting the greatest viability overall. This finding indicates that during the extended culture period, accompanied by medium replacement and the consequent decline in Sit concentration, cellular viability improved. Indeed, while the rapid release of Sit and the resulting sudden elevation of its concentration in the medium negatively affected fibroblast proliferation, a slower release profile maintaining lower concentrations favored cell growth. In line with our findings, previous studies have demonstrated that Sit enhances cell viability by reducing oxidative stress and ROS-mediated cytotoxicity, thereby exerting protective effects [62, 63]. The morphology of cells adhered to the surface of different wound dressings after 24 hours of culture is presented in Figure 6b. Cells on the Spg1 exhibited minimal adhesion, with sparse distribution and limited surface interaction. Incorporation of Fc-Ch nanoparticles improved cell compatibility and adhesion likely by balancing surface charge, introducing bioactive functional groups, and providing nanoscale topography [64, 65]. On the Spg2 and Spg3, cells exhibited better adhesion compared to Spg1; however, they still maintained a rounded morphology and formed cluster-like aggregates, indicating suboptimal spreading and substrate affinity. In contrast, the nanofibrous layer of the Dual-layer dressing supported extensive cell adhesion and spreading, with cells displaying flattened morphologies and intimate contact with the SF nanofibers. This behavior reflects the ECM-mimicking architecture of electrospun SF, which promotes cellular anchorage and surface coverage essential for early wound healing [66].

3.6. *In vivo* wound healing

The progression of diabetic wound closure was evaluated in the control group and treatment groups receiving the fabricated wound dressings over a 14‑day period. Representative macroscopic images of the wound surfaces in each group, together with the quantitative graph of wound closure rates, are presented in Figure 7. On day 7, no significant difference in wound closure was observed between the control group and the Spg1 group ($p > 0.05$), whereas the other groups demonstrated a significantly accelerated healing compared to the control ($p < 0.05$). Over the 14‑day period, all treatment groups exhibited significantly greater wound closure compared to the control ($p < 0.05$). Wound dressings containing Sit‑loaded Fc‑Ch nanoparticles markedly accelerated healing relative to the Spg1 and Spg2 dressings ($p < 0.001$), with the Dual‑layer group achieving the highest wound closure rate at both day 7 and day 14, thereby underscoring the critical role of the nanofibrous layer in accelerating wound repair. To further evaluate the healing process in the diabetic rat wound model, histopathological analyses were performed on tissue specimens harvested at day 14, enabling comparison of re-epithelialization, granulation tissue formation, and collagen deposition among the groups. In Figure 8a, H&E‑stained tissue sections are presented, allowing assessment of the wound healing process and evaluation of epidermal alterations as well as the formation of cutaneous appendages. The findings indicate that in the control group, even after 14 days, the epidermal layer (Ep.D) had not yet formed, and the wound surface remained largely covered by a blood crust. Moreover, abundant neovascular (N.V) structures and inflammatory cells (If.Cs) were clearly evident throughout the tissue. The abundant N.Vs observed indicates an active angiogenic phase, supporting tissue repair through oxygen and nutrient supply as well as immune cell recruitment. Overall, these findings suggest that in the control group the inflammatory phase persisted, and wound healing had only just initiated after 14 days. In the Spg1 group, the Ep.D layer was partially formed across the wound surface, with only a small portion of crust remaining at the wound center. The number of N.Vs and If.Cs was reduced, indicating an earlier onset of the proliferative phase and diminished inflammation compared to the control group. In groups treated with the Spg2, the Ep.D layer was completely formed, with only a minor crust observed at the wound center. The reduced presence of N.Vs and If.Cs

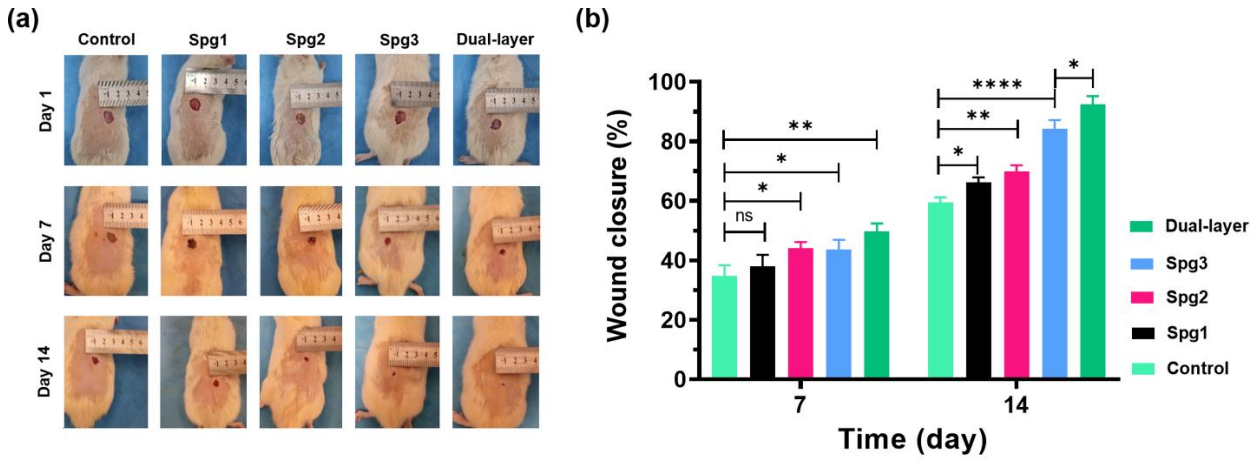

Figure 7. (a) Representative macroscopic images of wound surfaces in different groups over the 14‑day period; (b) quantitative graph of wound closure rates in each group. Significant differences are marked as "ns: not significant, *: $p < 0.05$, **: $p < 0.01$, and ****: $p < 0.0001$"

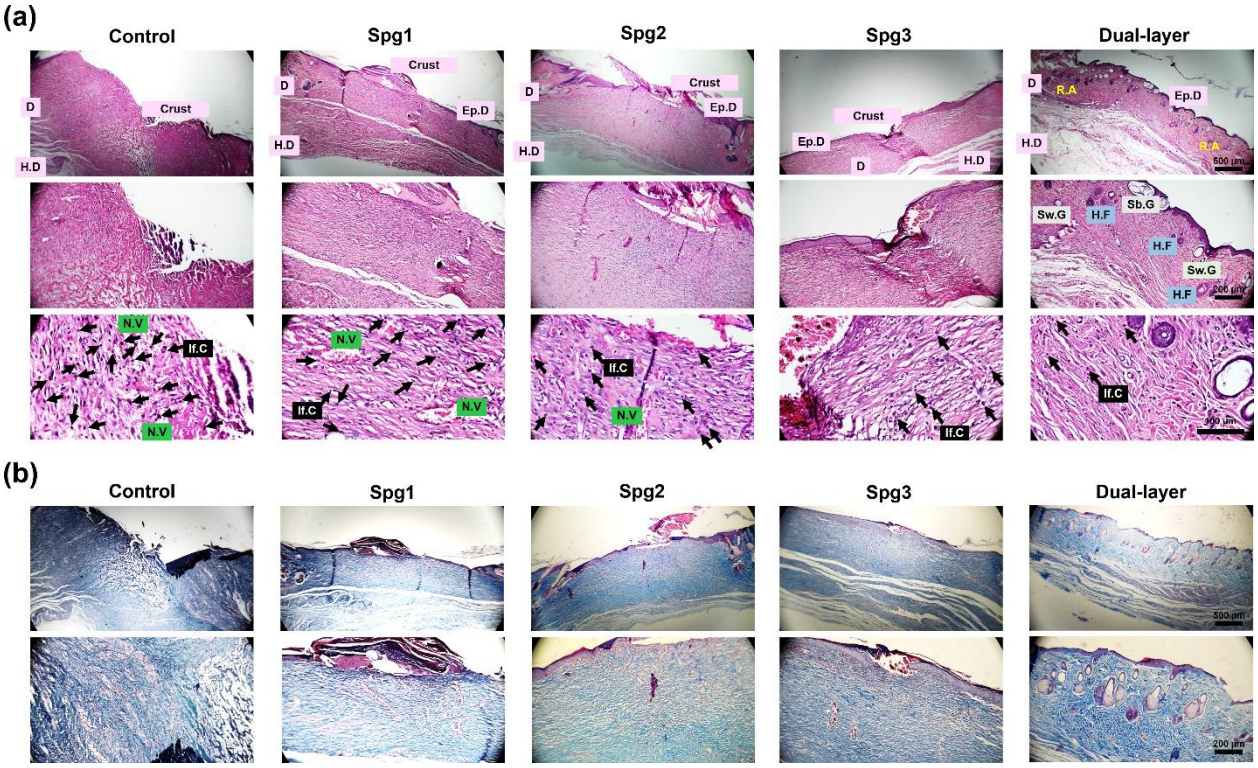

Figure 8. Histological evaluation of wound healing in different groups after 14 days. (a) H&E‑stained tissue sections; and (b) Masson's Trichrome‑stained tissue sections. Black arrows indicate inflammatory cells (If.C). Epidermis (Ep.D), dermis (D), hypodermis (H.D), regenerated area (R.A), inflammatory cells (If.C), neovascular structures (N.V), blood crust (Crust), hair follicles (H.F), sweat glands (Sw.G), and sebaceous glands (Sb.G) are marked on the images

10.57647/pibm.2025.1404.62

suggested that the angiogenic phase had been surpassed and that the healing process had markedly progressed. In the Spg3 group, a continuous Ep.D layer was established across the wound surface, while the amount of crust was markedly reduced compared with the Spg2 and Spg1. Histological evaluation showed N.Vs and If.Cs were scarcely detectable in the Spg3 group, indicating angiogenesis regression and progression toward near‑complete wound healing. In the Dual‑layer group, the Ep.D layer was completely formed with greater thickness compared to the other groups. The presence of N.Vs and If.Cs was markedly reduced and observed only in limited numbers. Remarkably, cutaneous appendages such as sweat glands (Sw.G), sebaceous glands (Sb.G), and particularly hair follicles (H.F) were abundantly detected within the regenerated area (R.A). Overall, the full development of the Ep.D layer, together with the presence of cutaneous appendages and H.Fs, and the absence of extensive N.V structures, indicates the termination of the wound healing phase in this group. Figure 8b presents histological sections of the groups following Masson's Trichrome staining, enabling evaluation of collagen organization and matrix status during wound repair. In the Control, Spg1, and Spg2 groups, collagen fibers appeared sparse, irregular, and loosely distributed (particularly in Control and Spg1) reflecting limited progression of the healing process. In contrast, the Spg3 and especially the Dual‑layer group exhibited densely packed and well‑organized collagen bundles within the dermal (D) layer. This organization was consistent with the development of the Ep.D layer and the reappearance of cutaneous appendages, collectively indicating high‑quality reconstruction of the skin architecture. The expression of VEGF and TGF-β, representing key regulators of angiogenesis and tissue regeneration, together with TNF-α and IL-1β, as major inflammatory cytokines, was evaluated by qRT-PCR on day 7 to provide insight into the early phase of wound healing. The results in Figure 9 clearly demonstrated that treatment groups generally exhibited higher expression of repair-associated genes compared to the control. However, VEGF expression in the Spg1 was not significantly different from the control ($p > 0.05$). In contrast, the Spg3 and Dual-layer groups showed markedly elevated VEGF expression relative to the other groups, although no significant difference was observed between these two groups ($p > 0.05$). Also, TGF-β expression was enhanced in both the Spg3 and Dual-layer groups; however, the Dual-layer formulation induced a significantly greater increase in TGF-β expression compared to the Spg3 ($p < 0.05$). It is noteworthy that the expression level of VEGF in the Spg2 group was statistically significantly higher compared to the Spg1 ($p<0.01$). Although the expression of the pro-inflammatory cytokine TNF-α did not differ significantly between the Spg1 and the control group ($p > 0.05$), all other treatment groups exhibited markedly reduced TNF-α levels compared to the control ($p <0.05$). The lowest expression values were observed in the Dual-layer and Spg3 groups ($p < 0.0001$ compared with the control), with no significant difference detected between them ($p > 0.05$). Similarly, IL-1β expression in all treatment groups was significantly lower than that of the control, with the lowest level observed in the Dual-layer group ($p < 0.0001$ compared to the control). These results clearly indicate that the presence of Fc-Ch nanoparticles within the dressings and the release of Sit from them played a pivotal role in promoting angiogenesis, enhancing tissue repair, and reducing wound inflammation. Moreover, the presence of a nanofibrous layer mimicking the ECM further boosted the regenerative effect and contributed to a more pronounced reduction in inflammation. The anti-inflammatory properties and angiogenic stimulation induced by Ch and Fc have been repeatedly reported in previous studies [65, 67-69]. It has also been reported that Sit can enhance the expression of angiogenic factors, including VEGF, thereby promoting angiogenic activity through the stimulation of endothelial progenitor cells [70]. Furthermore, Sit exerts a potent anti-inflammatory effect by suppressing CD26/DPP-IV expression and reducing proinflammatory cytokines, receptors, and kinases such as TNF-α, TLRs, JNK-1, and IKKβ [71]. In addition to these factors, the presence of a biomimetic SF nanofibrous layer resembling the ECM, which enhances cell proliferation and adhesion, enabled the Dual-layer dressing to exhibit the most effective performance in diabetic wound healing among all the dressings studied, specifically through the regulation of inflammation and the promotion of angiogenesis. Importantly, these findings highlight the translational potential of the Dual-layer construct as a multifunctional wound dressing that integrates exudate absorption, sustained drug delivery, and ECM mimicry, thereby addressing key clinical challenges in diabetic wound management. Nevertheless, certain limitations remain, including the lack of precise quantification of Sit concentrations in the wound microenvironment, the absence of *in vivo* release studies, and the need for systematic evaluation of safe and cytotoxic drug levels.

10.57647/pibm.2025.1404.62

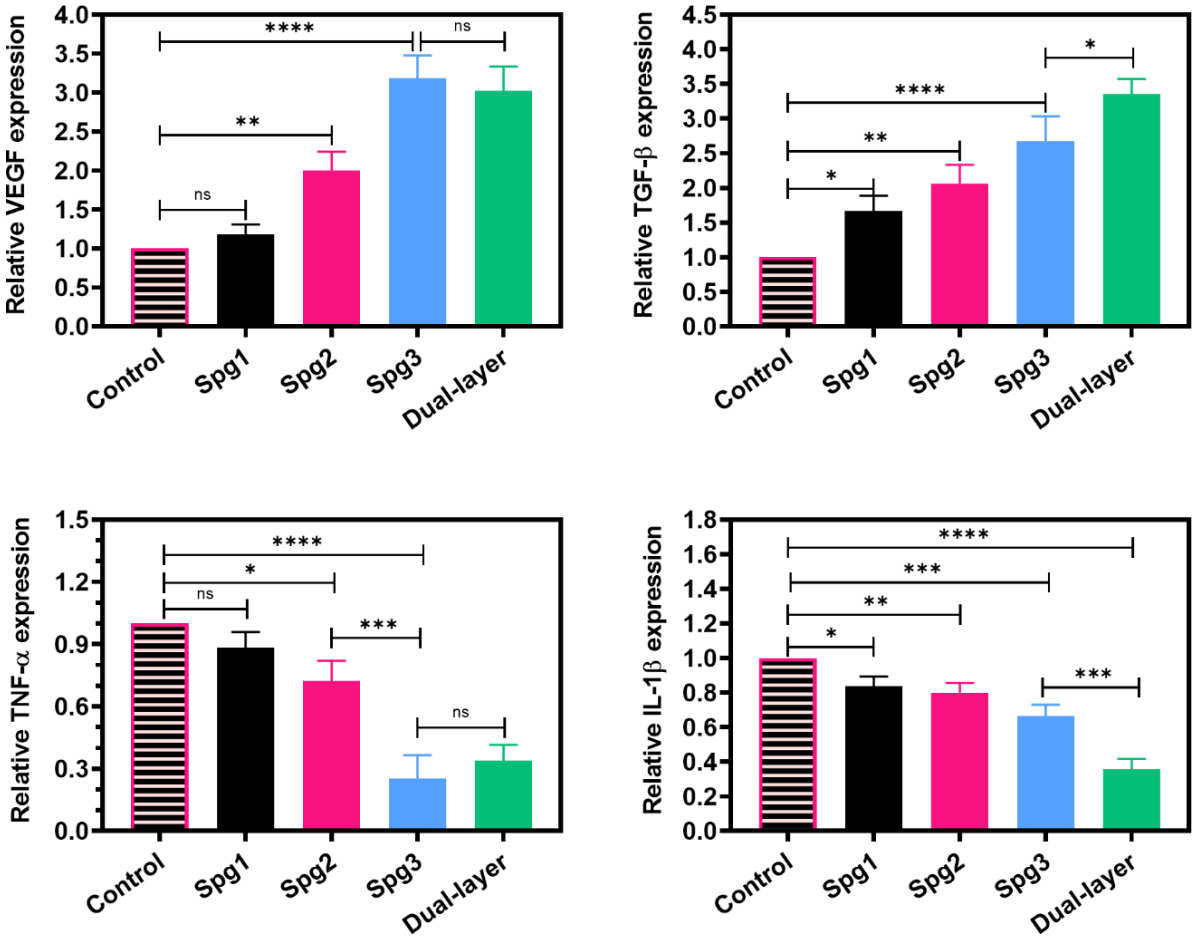

Figure 9. Gene expression levels of VEGF, TGF-β, TNF-α, and IL-1β, in different treatment groups on day 7, analyzed by qRT-PCR. Significant differences are marked as "ns: not significant, *: $p < 0.05$, **: $p < 0.01$, ***: $p < 0.001$, and ****: $p < 0.0001$"

4. Conclusion

In this study, the Spg1, Spg2, Spg3, and Dual-layer dressings were successfully fabricated with the aim of enhancing wound healing and accelerating the repair process in diabetic wounds. These dressings were systematically evaluated in terms of physicochemical, mechanical, and biological properties. All formulations demonstrated appropriate moisture absorption and biocompatibility, while the Dual-layer construct exhibited superior swelling behavior and mechanical properties. Sustained release of Sit from the Dual-layer dressing continued up to day 7. *In vitro* cellular assays confirmed enhanced L929 cell viability and adhesion, particularly supported by the nanofibrous layer. *In vivo* experiments revealed accelerated re-epithelialization and organized collagen deposition in the Dual-layer dressing treated group during 14 days, which was facilitated by early-stage angiogenesis and reduced inflammation. The Dual-layer wound dressing, integrating nanoparticle-mediated drug delivery within a sponge matrix and nanofibrous ECM mimicry, demonstrated superior physicochemical, mechanical, and biological performance, establishing it as a highly promising candidate for advanced wound healing applications, particularly in diabetic wounds. Importantly, the novelty of this work lies in the unique dual-layer architecture that combines a polyelectrolyte sponge matrix embedded with sitagliptin-loaded nanoparticles, together with an electrospun SF nanofibrous layer that mimics ECM properties. This synergistic integration provides a comparative advantage over conventional single-layer dressings by simultaneously addressing exudate absorption, drug delivery, and cellular interactions. Nevertheless, this study has certain limitations, and future investigations should systematically evaluate varying drug concentrations and nanoparticle formulations, explore alternative structural configurations, and include comprehensive *in vitro* and *in vivo* drug release studies

as well as determination of safe and cytotoxic Sit concentrations for target cells to further optimize therapeutic efficacy.

Authors contributions
All authors contributed equally to the conception, design, execution, and writing of this work. All authors read and approved the final manuscript.

Availability of data and materials
The datasets generated during and/or analyzed during the current study are available from the corresponding author on reasonable request.

Conflict of interests
The authors declare that they have no known competing financial interests or personal relationships that could have appeared to influence the work reported in this paper.

References

[1] Li, C., Jiang, T., Zhou, C., Jiang, A., Lu, C., Yang, G., Nie, J., Wang, F., Yang, X. and Chen, Z. 2023. Injectable self-healing chitosan-based POSS-PEG hybrid hydrogel as wound dressing to promote diabetic wound healing, *Carbohydrate Polymers*, 299, p. 120198.

[2] Ko, A. and Liao, C. 2023. Hydrogel wound dressings for diabetic foot ulcer treatment: status-quo, challenges, and future perspectives, *BMEMat*, 1, p. e12037.

[3] Khaliq, T., Sohail, M., Minhas, M.U., Mahmood, A., Munir, A., Qalawlus, A.H.M., Jabeen, N., Kousar, M. and Anwar, Z. 2023. Hyaluronic acid/alginate-based biomimetic hydrogel membranes for accelerated diabetic wound repair, *International Journal of Pharmaceutics*, 643, p. 123244.

[4] Shariatzadeh, F.J., Currie, S., Logsetty, S., Spiwak, R. and Liu, S. 2025. Enhancing wound healing and minimizing scarring: A comprehensive review of nanofiber technology in wound dressings, *Progress in Materials Science*, 147, p. 101350.

[5] Alizadeh, M., Salehi, S., Tavakoli, M., Mirhaj, M., Varshosaz, J., Kazemi, N., Salehi, S., Mehrjoo, M. and Abadi, S.A.M. 2023. PDGF and VEGF-releasing bi-layer wound dressing made of sodium tripolyphosphate crosslinked gelatin-sponge layer and a carrageenan nanofiber layer, *International Journal of Biological Macromolecules*, 233, p. 123491.

[6] Sarwar, M.S., Ghaffar, A., Huang, Q., Khalid, M., Anwar, A., Alayoubi, A.M. and Latif, M. 2023. Controlled drug release contenders comprising starch/poly (allylamine hydrochloride) biodegradable composite films, *International Journal of Biological Macromolecules*, 241, p. 124598.

[7] Sarwar, M.S., Huang, Q., Ghaffar, A., Abid, M.A., Zafar, M.S., Khurshid, Z. and Latif, M. 2020. A smart drug delivery system based on biodegradable chitosan/poly (allylamine hydrochloride) blend films, *Pharmaceutics*, 12, p. 131.

[8] Wang, M., Li, X., Hua, W., Shen, L., Yu, X. and Wang, X. 2016. Electrospun poly (acrylic acid)/silica hydrogel nanofibers scaffold for highly efficient adsorption of lanthanide ions and its photoluminescence performance, *ACS Applied Materials & Interfaces*, 8, pp. 23995–24007.

[9] Arkaban, H., Barani, M., Akbarizadeh, M.R., Pal Singh Chauhan, N., Jadoun, S., Dehghani Soltani, M. and Zarrintaj, P. 2022. Polyacrylic acid nanoplatforms: antimicrobial, tissue engineering, and cancer theranostic applications, *Polymers*, 14, p. 1259.

[10] Bandeira, M., Chee, B.S., Frassini, R., Nugent, M., Giovanela, M., Roesch-Ely, M., Crespo, J.d.S. and Devine, D.M. 2021. Antimicrobial PAA/PAH electrospun fiber containing green synthesized zinc oxide nanoparticles for wound healing, *Materials*, 14, p. 2889.

[11] Zhao, J., Qiu, P., Wang, Y., Wang, Y., Zhou, J., Zhang, B., Zhang, L. and Gou, D. 2023. Chitosan-based hydrogel wound dressing: From mechanism to applications, a review, *International Journal of Biological Macromolecules*, 244, p. 125250.

[12] Sezer, A.D., Hatipoglu, F., Cevher, E., Oğurtan, Z., Bas, A.L. and Akbuğa, J. 2007. Chitosan film containing fucoidan as a wound dressing for dermal burn healing: preparation and in vitro/in vivo evaluation, *AAPS PharmSciTech*, 8, p. 39.

[13] Lu, Y., Zhu, X., Hu, C., Li, P., Zhao, M., Lu, J. and Xia, G. 2022. A fucoidan-gelatin wound dressing accelerates wound healing by enhancing antibacterial and anti-inflammatory activities, *International Journal of Biological Macromolecules*, 223, pp. 36–48.

[14] Egle, K., Dohle, E., Hoffmann, V., Salma, I., Al-Maawi, S., Ghanaati, S. and Dubnika, A. 2024. Fucoidan/chitosan hydrogels as carrier for sustained delivery of platelet-rich fibrin containing bioactive molecules, *International Journal of Biological Macromolecules*, 262, p. 129651.

[15] Heydari Foroushani, P., Rahmani, E., Alemzadeh, I., Vossoughi, M., Pourmadadi, M., Rahdar, A. and Díez-Pascual, A.M. 2022. Curcumin sustained release with a hybrid chitosan-silk fibroin nanofiber containing silver nanoparticles as a novel highly efficient antibacterial wound dressing, *Nanomaterials*, 12, p. 3426.

[16] Aldahish, A., Shanmugasundaram, N., Vasudevan, R., Alqahtani, T., Alqahtani, S., Mohammad Asiri, A., Devanandan, P., Thamaraikani, T., Vellapandian, C. and Jayasankar, N. 2024. Silk fibroin nanofibers: advancements in bioactive dressings through electrospinning technology for diabetic wound healing, *Pharmaceuticals*, 17, p. 1305.

[17] Al-Musawi, M.H., Turki, S., Al-Naymi, H.A.S., Al-salman, S.S., Boroujeni, V.V., Alizadeh, M., Sattar, M., Sharifianjazi, F., Bazli, L. and Pajooh, A.M.D. 2024. Localized delivery of healing stimulator medicines for enhanced wound treatment, *Journal of Drug Delivery Science and Technology*, 101, p. 106212.

[18] Liu, X., Zhang, T. and Zhang, C. 2020. Sitagliptin inhibits extracellular matrix accumulation and proliferation in lung fibroblasts, Medical Science Monitor: *International Medical Journal of Experimental and Clinical Research*, 26, p. e922644.

[19] Angadi, N.B., Kagal, U. and Timshetti, S. 2018. Effect of sitagliptin and vildagliptin on wound healing in male wistar rats–an experimental study, *Asian Journal of Pharmacy and Clinical Research*, 11, pp. 392–394.

[20] Xiang, G., Huang, X., Wang, T., Wang, J., Zhao, G., Wang, H., Feng, Y., Lei, W. and Hu, X. 2020. The impact of sitagliptin on macrophage polarity and angiogenesis in the osteointegration of titanium implants in type 2 diabetes, *Biomedicine & Pharmacotherapy*, 126, p. 110078.

[21] SreeHarsha, N., Ramnarayanan, C., Al-Dhubiab, B.E., Nair, A.B., Hiremath, J.G., Venugopala, K.N., Satish, R.T., Attimarad, M. and Shariff, A. 2019. Mucoadhesive Particles: A Novel,

Prolonged-Release Nanocarrier of Sitagliptin for the Treatment of Diabetics, *BioMed Research International*, 2019, p. 3950942.

[22] Haq Asif, A., Harsha, S., Hodalur Puttaswamy, N. and E. Al-Dhubiab, B. 2018. An effective delivery system of sitagliptin using optimized mucoadhesive nanoparticles, *Applied Sciences*, 8, p. 861.

[23] Elbadr, M.M., Galal, H.A., Hetta, H.F., Elfadil, H., Alanazi, F.E., Fawzy, S., Aljohani, H.M., Abd Ellah, N.H., Ali, M.F. and Dyab, A.K. 2025. Immunomodulatory Effect of Rivaroxaban Nanoparticles Alone and in Combination with Sitagliptin on Diabetic Rat Model, *Diseases*, 13, p. 87.

[24] Barbosa, A.I., Costa Lima, S.A. and Reis, S. 2019. Application of pH-responsive fucoidan/chitosan nanoparticles to improve oral quercetin delivery, *Molecules*, 24, p. 346.

[25] Coutinho, A.J., Lima, S.A.C., Afonso, C.M. and Reis, S. 2020. Mucoadhesive and pH responsive fucoidan-chitosan nanoparticles for the oral delivery of methotrexate, *International Journal of Biological Macromolecules*, 158, pp. 180–188.

[26] Wilson, B., Alobaid, B.N.M., Geetha, K.M. and Jenita, J.L. 2021. Chitosan nanoparticles to enhance nasal absorption and brain targeting of sitagliptin to treat Alzheimer's disease, *Journal of Drug Delivery Science and Technology*, 61, p. 102176.

[27] George, A. and Shrivastav, P.S. 2023. Preparation and optimization of tetraethyl orthosilicate cross-linked chitosan-guar gum-poly (vinyl alcohol) composites reinforced with montmorillonite for sustained release of sitagliptin, *International Journal of Biological Macromolecules*, 229, pp. 51–61.

[28] Khalatbari, E., Tajabadi, M. and Khavandi, A. 2022. Multifunctional exosome-loaded silk fibroin/alginate structure for potential wound dressing application, *Materials Today Communications*, 31, p. 103549.

[29] Hadisi, Z., Farokhi, M., Bakhsheshi-Rad, H.R., Jahanshahi, M., Hasanpour, S., Pagan, E., Dolatshahi-Pirouz, A., Zhang, Y.S., Kundu, S.C. and Akbari, M. 2020. Hyaluronic acid (HA)-based silk fibroin/zinc oxide core–shell electrospun dressing for burn wound management, *Macromolecular Bioscience*, 20, p. 1900328.

[30] Bidaki, A., Rezaei, N., Kazemi, S., Ali, S.N., Ziaei, S., Moeinzadeh, A., Hosseini, F., Noorbazargan, H., Farmani, A.R. and Ren, Q. 2025. 3D printed bioengineered scaffold containing chitosan, alginate, and Barijeh-loaded niosomes enabled efficient antibiofilm activity and wound healing, *International Journal of Biological Macromolecules*, p. 143743.

[31] Dash, S. 2010. Kinetic modeling on drug release from controlled drug delivery systems, *Acta Poloniae Pharmaceutica*.

[32] Wójcik-Pastuszka, D., Krzak, J., Macikowski, B., Berkowski, R., Osiński, B. and Musiał, W. 2019. Evaluation of the release kinetics of a pharmacologically active substance from model intra-articular implants replacing the cruciate ligaments of the knee, *Materials*, 12, p. 1202.

[33] Nokoorani, Y.D., Shamloo, A., Bahadoran, M. and Moravvej, H. 2021. Fabrication and characterization of scaffolds containing different amounts of allantoin for skin tissue engineering, *Scientific Reports*, 11, p. 16164.

[34] Preet, S., Sharma, S., Panjeta, A., Kaur, J., Alshammari, A., Alharbi, M. and Almawash, S. 2022. Accelerated Wound Healing Potential of Nisin in Streptozotocin Induced Diabetes Mellitus in Wistar Rats, *International Journal of Peptide Research and Therapeutics*, 28, p. 147.

[35] Nasiry, D., Khalatbary, A.R., Noori, A., Abouhamzeh, B. and Jamalpoor, Z. 2023. Accelerated wound healing using three-dimensional amniotic membrane scaffold in combination with adipose-derived stem cells in a diabetic rat model, *Tissue and Cell*, 82, p. 102098.

[36] Rahmani, H., Fattahi, A., Sadrjavadi, K., Khaledian, S. and Shokoohinia, Y. 2019. Preparation and characterization of silk fibroin nanoparticles as a potential drug delivery system for 5-fluorouracil, *Advanced Pharmaceutical Bulletin*, 9, p. 601.

[37] Trenkenschuh, E. and Friess, W. 2021. Freeze-drying of nanoparticles: How to overcome colloidal instability by formulation and process optimization, *European Journal of Pharmaceutics and Biopharmaceutics*, 165, pp. 345–360.

[38] Maldiney, T., Viana, B., Bessière, A., Gourier, D., Bessodes, M., Scherman, D. and Richard, C. 2013. In vivo imaging with persistent luminescence silicate-based nanoparticles, *Optical Materials*, 35, pp. 1852–1858.

[39] Barbosa, A.I., Lima, S.A.C. and Reis, S. 2019. Development of methotrexate loaded fucoidan/chitosan nanoparticles with anti-inflammatory potential and enhanced skin permeation, *International Journal of Biological Macromolecules*, 124, pp. 1115–1122.

[40] Venkatesan, J., Singh, S.K., Anil, S., Kim, S.-K. and Shim, M.S. 2018. Preparation, characterization and biological applications of biosynthesized silver nanoparticles with chitosan-fucoidan coating, *Molecules*, 23, p. 1429.

[41] Rajendran, N.K., Kumar, S.S.D., Houreld, N.N. and Abrahamse, H. 2018. A review on nanoparticle based treatment for wound healing, *Journal of Drug Delivery Science and Technology*, 44, pp. 421–430.

[42] Samourides, A., Anayiotos, A., Kapnisis, K., Xenou, Z., Hearnden, V. and Chen, B. 2021. Fabrication of hierarchical multilayer poly (glycerol sebacate urethane) scaffolds based on ice-templating, *Applied Sciences*, 11, p. 5004.

[43] Lee, S.M., Park, I.K., Kim, Y.S., Kim, H.J., Moon, H., Mueller, S. and Jeong, Y.-I. 2016. Physical, morphological, and wound healing properties of a polyurethane foam-film dressing, *Biomaterials Research*, 20, p. 15.

[44] Shi, Y., Zhang, H., Zhang, X., Chen, Z., Zhao, D. and Ma, J. 2020. A comparative study of two porous sponge scaffolds prepared by collagen derived from porcine skin and fish scales as burn wound dressings in a rabbit model, *Regenerative Biomaterials*, 7, pp. 63–70.

[45] Rasoulianboroujeni, M., Kiaie, N., Tabatabaei, F.S., Yadegari, A., Fahimipour, F., Khoshroo, K. and Tayebi, L. 2018. Dual porosity protein-based scaffolds with enhanced cell infiltration and proliferation, *Scientific Reports*, 8, p. 14889.

[46] Mukasheva, F., Adilova, L., Dyussenbinov, A., Yernaimanova, B., Abilev, M. and Akilbekova, D. 2024. Optimizing scaffold pore size for tissue engineering: Insights across various tissue types, *Frontiers in Bioengineering and Biotechnology*, 12, p. 1444986.

[47] Itano, K., Choi, J. and Rubner, M.F. 2005. Mechanism of the pH-induced discontinuous swelling/deswelling transitions of poly (allylamine hydrochloride)-containing polyelectrolyte multilayer films, *Macromolecules*, 38, pp. 3450–3460.

[48] Jozaghkar, M.R., Sepehrian Azar, A. and Ziaee, F. 2023. Synthesis and characterization of semi-interpenetrating polymer network hydrogel based on polyacrylic acid/polyallylamine and its application in wastewater remediation, *Polymer Bulletin*, 80, pp. 2119–2135.

[49] Tavakoli, M., Karbasi, S. and Soleymani Eil Bakhtiari, S. 2020. Evaluation of physical, mechanical, and biodegradation of chitosan/graphene oxide composite as bone substitutes, *Polymer-Plastics Technology and Materials*, 59, pp. 430–440.

[50] Ho, T.T., Bremmell, K.E., Krasowska, M., MacWilliams, S.V., Richard, C.J., Stringer, D.N. and Beattie, D.A. 2015. In situ ATR FTIR spectroscopic study of the formation and hydration of a fucoidan/chitosan polyelectrolyte multilayer, *Langmuir*, 31, pp. 11249–11259.

[51] Zhang, H., Li, L.-l., Dai, F.-y., Zhang, H.-h., Ni, B., Zhou, W., Yang, X. and Wu, Y.-z. 2012. Preparation and characterization of silk fibroin as a biomaterial with potential for drug delivery, *Journal of Translational Medicine*, 10, p. 117.

[52] Cui, R., Zhang, L., Ou, R., Xu, Y., Xu, L., Zhan, X.-Y. and Li, D. 2022. Polysaccharide-based hydrogels for wound dressing: Design considerations and clinical applications, *Frontiers in Bioengineering and Biotechnology*, 10, p. 845735.

[53] Sanjay, S.T., Zhou, W., Dou, M., Tavakoli, H., Ma, L., Xu, F. and Li, X. 2018. Recent advances of controlled drug delivery using microfluidic platforms, *Advanced Drug Delivery Reviews*, 128, pp. 3–28.

[54] Adepu, S. and Ramakrishna, S. 2021. Controlled drug delivery systems: current status and future directions, *Molecules*, 26, p. 5905.

[55] Gasner, P., Babusca, D., Vleoanga, A. and Dorohoi, D.O. 2025. Korsmeyer–Peppas Model for Diacetylaminoazotoluene (Dimazon) Release from PVA Foils: A Spectral Study, *Symmetry*, 17, p. 1739.

[56] Gefen, A., Alves, P., Beeckman, D., Lázaro-Martínez, J.L., Lev-Tov, H., Najafi, B., Swanson, T. and Woo, K. 2023. Mechanical and contact characteristics of foam materials within wound dressings: Theoretical and practical considerations in treatment, *International Wound Journal*, 20, pp. 1960–1978.

[57] Cheng, Y., Koh, L.-D., Li, D., Ji, B., Han, M.-Y. and Zhang, Y.-W. 2014. On the strength of β-sheet crystallites of Bombyx mori silk fibroin, *Journal of the Royal Society Interface*, 11, p. 20140305.

[58] Mohandas, A., Nimal, T., Das, V., Shankarappa, S.A., Biswas, R. and Jayakumar, R. 2015. Drug loaded bi-layered sponge for wound management in hyperfibrinolytic conditions, *Journal of Materials Chemistry B*, 3, pp. 5795–5805.

[59] Sudheesh Kumar, P., Lakshmanan, V.-K., Anilkumar, T., Ramya, C., Reshmi, P., Unnikrishnan, A., Nair, S.V. and Jayakumar, R. 2012. Flexible and microporous chitosan hydrogel/nano ZnO composite bandages for wound dressing: in vitro and in vivo evaluation, *ACS Applied Materials & Interfaces*, 4, pp. 2618–2629.

[60] Long, H., Ma, K., Xiao, Z., Ren, X. and Yang, G. 2017. Preparation and characteristics of gelatin sponges crosslinked by microbial transglutaminase, *PeerJ*, 5, p. e3665.

[61] Jiang, Y., Yao, Y., Li, J., Wang, Y., Cheng, J. and Zhu, Y. 2021. Functional dissection of CD26 and its pharmacological inhibition by sitagliptin during skin wound healing, *Medical Science Monitor: International Medical Journal of Experimental and Clinical Research*, 27, p. e928933.

[62] Yang, M., Xi, N., Gao, M. and Yu, Y. 2022. Sitagliptin mitigates hypoxia/reoxygenation (H/R)-induced injury in cardiomyocytes by mediating sirtuin 3 (SIRT3) and autophagy, *Bioengineered*, 13, pp. 13162–13173.

[63] Cao, Q., Xu, D., Chen, Y., Long, Y., Dai, F., Gui, L. and Lu, Y. 2021. Sitagliptin reduces endothelial dysfunction and apoptosis induced by high-fat diet and palmitate in thoracic aortas and endothelial cells via ROS-ER stress-CHOP pathway, *Frontiers in Pharmacology*, 12, p. 670389.

[64] Barbosa, A.I., Coutinho, A.J., Costa Lima, S.A. and Reis, S. 2019. Marine polysaccharides in pharmaceutical applications: Fucoidan and chitosan as key players in the drug delivery match field, *Marine Drugs*, 17, p. 654.

[65] Abbas, M.F., Karim, D.K., Kareem, H.R., Kamil, M.M., Al-Musawi, M.H., Asker, M.H., Ghanami, M., Shahriari-Khalaji, M., Sattar, M. and Mirhaj, M. 2025. Fucoidan and its derivatives: From extraction to cutting-edge biomedical applications, *Carbohydrate Polymers*, p. 123468.

[66] Dai, S., Liang, H., Zhu, M. and Zhang, Y. 2024. Electrospun silk for biomedical applications, *Med-X*, 2, p. 22.

[67] Maita, K.C., Avila, F.R., Torres-Guzman, R.A., Garcia, J.P., Eldaly, A.S., Palmieri, L., Emam, O.S., Ho, O. and Forte, A.J. 2022. Local anti-inflammatory effect and immunomodulatory activity of chitosan-based dressing in skin wound healing: A systematic review, *Journal of Clinical and Translational Research*, 8, p. 488.

[68] Tan, Y., Xu, C., Liu, Y., Bai, Y., Li, X. and Wang, X. 2024. Sprayable and self-healing chitosan-based hydrogels for promoting healing of infected wound via anti-bacteria, anti-inflammation and angiogenesis, *Carbohydrate Polymers*, 337, p. 122147.

[69] Ahmad, T., Eapen, M.S., Ishaq, M., Park, A.Y., Karpiniec, S.S., Stringer, D.N., Sohal, S.S., Fitton, J.H., Guven, N. and Caruso, V. 2021. Anti-inflammatory activity of fucoidan extracts in vitro, *Marine Drugs*, 19, p. 702.

[70] Yu, G., Liu, P., Shi, Y., Li, S., Liu, Y. and Zhu, W. 2019. Sitagliptin stimulates endothelial progenitor cells to induce endothelialization in aneurysm necks through the SDF-1/CXCR4/NRF2 signaling pathway, *Frontiers in Endocrinology*, 10, p. 823.

[71] Makdissi, A., Ghanim, H., Vora, M., Green, K., Abuaysheh, S., Chaudhuri, A., Dhindsa, S. and Dandona, P. 2012. Sitagliptin exerts an antinflammatory action, *The Journal of Clinical Endocrinology & Metabolism*, 97, pp. 3333–3341.